A Variable Switching Frequency Multimode Control Scheme for Single-Phase Grid-Tied Multilevel PV Microinverters

Lyuyi Lin, *Student Member, IEEE*, Junming Zhang, *Senior Member, IEEE*, and Shuai Shao, *Member, IEEE*

***Abstract*—Single-phase grid-tied microinverters are required to operate over a wide power range in photovoltaic applications. It is desirable to improve the efficiency over the entire power range without extra cost. This article proposes a variable switching frequency (VSF) multimode control scheme to optimize the device losses at each operating point for a single-phase T-type hybrid-bridge inverter. The proposed optimal control scheme is devised based on the *V–I* plane analysis and can therefore be applied in both unity power factor (PF) and nonunity PF operations. With reasonable simplifications and curve fitting, neither a multidimensional lookup table nor excessive computational burden is required for the controller. A 1-kW prototype is built to verify the proposed optimal VSF scheme and compare it with the conventional constant switching frequency (CSF) scheme. The experimental results show that the proposed optimal VSF scheme can achieve higher efficiency than the CSF scheme over a wide power range. The weighted average efficiency of the proposed scheme is improved by a maximum of 1.3% in unity PF operation and 0.63% in nonunity PF operation.**

***Index Terms*—Loss optimization, multimode control, photovoltaic (PV), T-type inverter, variable switching frequency (VSF).**

I. Introduction

PHOTOVOLTAIC (PV) market is flourishing all over the world in the last few years and the capacity of residential PV is growing rapidly. Single-phase grid-tied microinverters are popular in residential PV systems due to their compact design, small mismatch loss, high reliability, and low installation cost. In PV systems, the output power of PV modules will vary with climatic conditions and solar irradiance. Thus, weighted average efficiencies, such as European (EU) efficiency or California Energy Commission (CEC) efficiency, are used to evaluate the performance of inverters. However, optimization based on the largest weighting factor of one standard may not perform well in another standard. According to a recent comparison of PV microinverters [5], some inverters ranked well at the CEC efficiency but dropped at the EU efficiency. Besides, most inverters suffer from low efficiency in light loads which affects the weighted efficiency. Therefore, inverter efficiency should be optimized not only at a single point but also over the full range of power.

As well known, inverters can operate in continuous conduction mode (CCM), discontinuous conduction mode (DCM), or boundary conduction mode (BCM). Usually, CCM is more suitable for heavy loads due to lower conduction loss, whereas DCM or BCM is preferred in low-power applications because of lower switching loss. BCM has been widely used in microinverters due to zero voltage switching (ZVS) merit but has the drawback of wide switching frequency range and high peak current. Since the instantaneous output power of the inverter always varies from no load to heavy load in each line cycle, it is very difficult to optimize the efficiency with a single control method. By operating in a proper mode as instantaneous power varies, which is called multimode control, it is possible to combine the advantages of different operation modes and improve overall efficiency. In [6], the converter operated between CCM and DCM with several given switching frequencies throughout the ac line cycle. In [7], the switching frequency is designed as a linear piecewise function of output current, which is far from the optimum. The research works in [8] and [9] combined BCM and nonoptimized constant switching frequency (CSF) DCM. Liu et al. [10] proposed a hybrid control scheme combining BCM and limited switching frequency triangular current mode (TCM). Although the switching frequency range is narrowed and full range ZVS is achieved, the current ripple is large and, thus, conduction loss and turn-OFF loss are still high.

In recent years, variable switching frequency (VSF) control schemes have attracted a lot of research interest to achieve ZVS [11] or to optimize current ripple distribution and reduce switching losses [12], [13], [14], [15], [16], [17], [18], [19]. A variable off-time control method is proposed by Zhang et al. [13] to increase efficiency at light load, which is essentially a VSF scheme. The research work in [14] implemented a VSF scheme by a constant frequency peak current controller. In [15], [16], and [17], VSF is proposed based on current ripple prediction and the peak of the current ripple is limited. VSF scheme is also adopted in [18] to minimize switching loss without increasing the rms of current ripple. An improved VSF method is proposed in [19] to find the balance between switching loss and core loss. However, in the aforementioned works, inverters are usually operated in

Manuscript received 15 October 2022; revised 14 February 2023 and 28 March 2023; accepted 5 May 2023. Date of publication 10 May 2023; date of current version 28 July 2023. This work was supported in part by the National Key Research and Development Program of China under Grant 2022YFE0205100 and in part by the Fundamental Research Funds for the Central Universities under Grant 226-2023-00052. Recommended for publication by Associate Editor D. Vinnikov. *(Corresponding author: Junming Zhang.)*

The authors are with the College of Electrical Engineering, Zhejiang University, Hangzhou 310058, China (e-mail: lin61@zju.edu.cn; zhangjm@zju.edu.cn; shaos@zju.edu.cn).

Color versions of one or more figures in this article are available at https://doi.org/10.1109/TPEL.2023.3274925.

Digital Object Identifier 10.1109/TPEL.2023.3274925

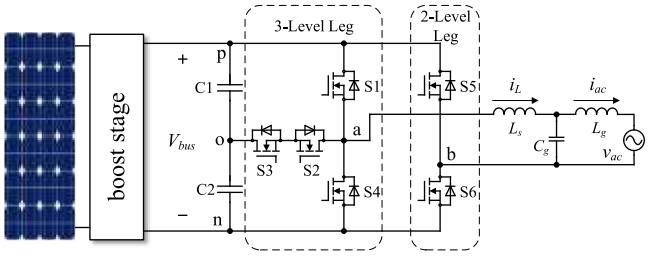

Fig. 1. Topology of T-type hybrid-bridge five-level inverter.

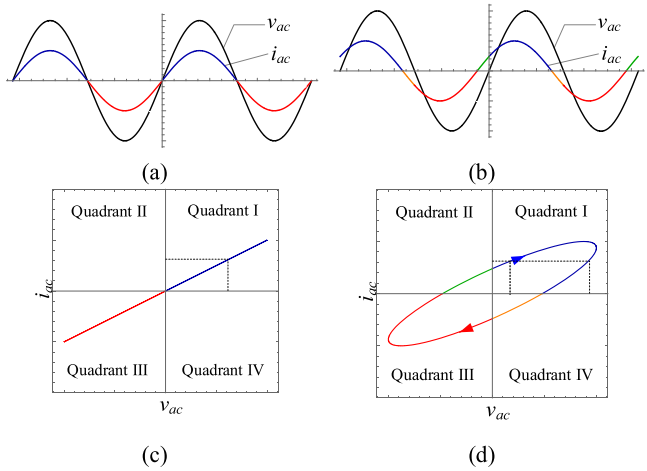

Fig. 2. Time-domain waveforms and state-plane trajectories of AC output. (a) $v_{\rm ac}$ and $i_{\rm ac}$ when PF = 1. (b) $v_{\rm ac}$ and $i_{\rm ac}$ when PF = 0.87, current leading. (c) Trajectory when PF = 1. (d) Trajectory when PF = 0.87, current leading.

only one or two modes, which are hard to optimize the overall power loss.

With the increasing power of PV modules, microinverters are expected to operate in a wider power range. It is desirable to adopt VSF in multimode control to further optimize the conduction loss and switching loss without additional hardware cost. Moreover, multilevel inverters have been developed in many PV applications [20], [21], [22] to improve efficiency and power density. For multilevel inverters, there might be more operating modes so that efficiency optimizations will be more complex.

To overcome these issues, this article proposes a VSF multimode control scheme for multilevel inverters, including both unity power factor (PF) and nonunity PF operation. Since the power loss of the switches is the dominant power loss of the inverter, the optimization in this work is carried out to minimize the conduction loss and switching loss of the power devices. The inductor loss is not considered in the optimization for simplicity. The optimization aims to find the optimal operating status, including optimal operating mode and optimal switching frequency, based on the instantaneous output voltage and output current information. Using the curve-fitting method, the proposed optimal control strategy can be easily implemented in the DSP controller with neither a heavy computational burden nor a multidimensional look-up table. A T-type hybrid-bridge topology is adopted as the power stage, and the experimental results show that the proposed VSF control scheme can save loss over the whole operating range and improve weighted average efficiency compared to the conventional CSF control scheme.

The rest of this article is organized as follows. Section II introduces the *V–I* plane trajectory of inverter ac output and analyzes the corresponding switching sequence in different regions on the *V–I* plane. The analysis showed that the optimal operating status can be calculated in a small region instead of the whole *V–I* plane. Section III derived the optimal operating status, which consists of the optimal mode (CCM, BCM, or DCM) and the optimal switching efficiency. The control strategy is obtained using the curve-fitting process. In Section IV, the implementation of the control system is discussed. In Section V, the simulation results on loss distribution and current distortion are presented. Finally, Section VI concludes this article.

II. *V–I* Plane Analysis

The following analysis is based on a T-type hybrid-bridge five-level inverter as shown in Fig. 1. A two-stage structure is widely adopted for PV microinverter applications [1], [23]. The boost stage realizes the function of maximum power point tracking, galvanic isolation, and voltage step-up. The inverter stage shapes the output current and injects it into the grid. The T-type hybrid-bridge inverter consists of two switching legs: one is the three-level T-type leg and the other is the two-level leg [24]. The T-type hybrid-bridge structure only requires six power devices, whereas the dual-bridge structure, which consists of two three-level legs, requires eight devices. Thus, the hybrid-bridge inverter has fewer power devices and lower conduction losses with the same voltage levels. Therefore, it is adopted here for the following analysis. The same concept can also be applied to other multilevel topologies.

To optimize the power loss of an inverter, it is more convenient and straightforward to minimize power loss at each operating point ($v_{\rm ac}$, $i_{\rm ac}$) than the average power loss during a line cycle. As long as the power loss at each operating point is minimized, the total loss over the entire operating range is also minimized. In this section, the inverter output trajectory on the *V–I* plane is introduced first. For nonunity PF operation, the inverter operates among different quadrants with different switching sequences. The loss calculation formula will also be different. The switching sequence in different regions on the *V–I* plane is analyzed to simplify the optimization.

A. *Inverter Output Trajectory on the* V–I *Plane*

The output of the inverter can be mapped as a trajectory on the *V–I* plane. Two examples are shown in Fig. 2. Fig. 2(a) shows the waveform of instantaneous output voltage $v_{\rm ac}$ and instantaneous output current $i_{\rm ac}$ in unity PF operation. The state-plane trajectory shown in Fig. 2(c) is a line segment, which indicates that the inverter will only operate in Quadrant I and III in unity PF operation. Fig. 2(b) shows the waveforms in nonunity PF operation where the output current has a leading phase as an example. As shown in Fig. 2(d), the trajectory for nonunity PF operation is an ellipse and the inverter will operate clockwise

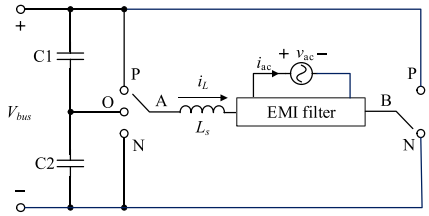

Fig. 3. Topology of T-type hybrid-bridge five-level inverter.

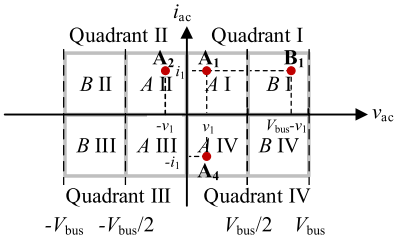

Fig. 4. Operating regions and the example operating points: A_1 (v_1, i_1), A_2 ($-v_1$, i_1), A_4 (v_1, $-i_1$), and B_1 (V_{bus}-v_1, i_1).

among four quadrants. It should be noted that if the PF is the same and the output current is lagging, the trajectory is the same as Fig. 2(d) but the inverter will operate counterclockwise.

According to Fig. 2, in unity PF operation, i_{ac} is a single-valued function of v_{ac}. Once i_{ac} is known, the operating point is determined and the switching frequency can be optimized. In this case, optimization only depends on the output current i_{ac} or the instantaneous output power. However, in nonunity PF operation, since i_{ac} is no longer a single-valued function of v_{ac}, optimization should be dependent on both i_{ac} and v_{ac}.

B. Switching Sequence in Different Regions on the V–I *Plane*

The switching sequences are different in different quadrants. Moreover, in a multilevel inverter, the switching sequences might change with the output voltage even operating in the same quadrant. Take the T-type hybrid-bridge inverter as an example. In Quadrant I, S1 and S2 switch complementarily when $v_{ac} > V_{bus}/2$ whereas S3 and S4 switch complementarily when $v_{ac} < V_{bus}/2$. It is complicated to find the optimal switching frequency at every operating point on the whole *V–I* plane. Thus, the following analysis will discuss the switching sequence in different regions and simplify the problem.

The simplified schematic of the T-type hybrid-bridge inverter is shown in Fig. 3. The three-level leg is represented by switch A, and the two-level leg is represented by switch B. The node voltage V_A switches among V_P, V_O, and V_N, whereas V_B switches among V_P and V_N. The inductor current waveform in the following analysis is considered to be triangular.

For five-level inverters, operation on the *V–I* plane can be divided into eight regions, which is shown in Fig. 4. The switching sequences are different depending on the operating region. Four example operating points are analyzed, which are plotted in Fig. 4. The analysis of operating points in other regions can be obtained by symmetry and therefore is not discussed.

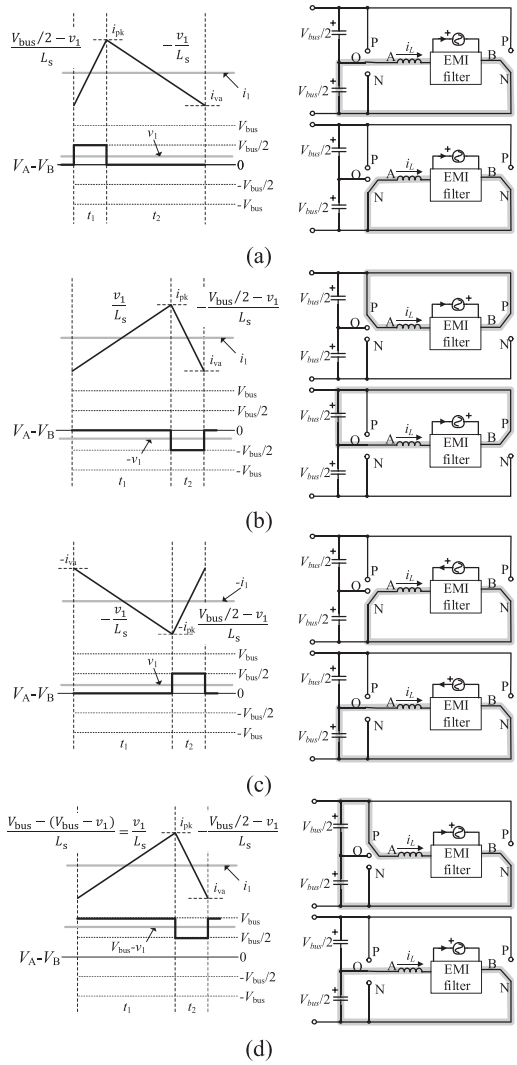

Fig. 5. Inductor current waveform and current path at operating point: (a) A_1 (v_1, i_1), (b) A_2 ($-v_1$, i_1), (c) A_4 (v_1, $-i_1$), and (d) B_1 (V_{bus}-v_1, i_1).

1) Operating Point A_1 (v_1, i_1) in Region A *I ($0 < v_1 < V_{bus}/2$):* At this operating point, switch B is always connected to node N, and switch A switches between node O and N. Assume the inverter operates in CCM, the inductor current waveform is indicated in Fig. 5(a). In a switching cycle, the inductor current rises during interval t_1 and falls during interval t_2. The differential voltage of the two legs, V_A–V_B, equals to $V_{bus}/2$ during t_1 and 0 during t_2. The slope of the inductor current is given and labeled in Fig. 5(a).

2) Operating Point A_2 ($-v_1$, i_1) in Region A *II:* This operating point is in Quadrant II, the so-called "negative power region," where the output voltage is negative and the output current is positive. This operation mode only occurs in nonunity PF cases. The inductor current waveform and the related current slope are indicated in Fig. 5(b). On comparing Fig. 5(b) with Fig. 5(a), it can be found that the inductor current waveform at A_2 is the mirror of that at A_1. Since the instantaneous output currents at these two points are all i_1, the peak current i_{pk} and the valley current i_{va} at A_1 and A_2 are the same at a certain switching

frequency. As a result, the conduction loss and the switching loss of these two operating points are the same.

3) Operating Point A_4 (v_1, $-i_1$) in Region A IV: As for operating point A_4 in Quadrant IV, the output current is negative and output voltage remains positive. The inductor current waveform and the slope in each interval is shown in Fig. 5(c). The waveform at A_4 is the 180° rotation of the waveform at A_1 and the absolute values of instantaneous output current at these two points are the same. Similar to the previous analysis, the absolute peak current and valley current, the conduction loss, and the switching loss are the same for a given switching frequency.

4) Operating Point B_1 (V_{bus}-v_1, i_1) in Region B I: Operating points B_1 and A_1 are symmetric about $v_{\rm ac} = V_{\rm bus}/2$ as shown in Fig. 4. The inductor current waveform is shown in Fig. 5(d), which is the same as the waveform at A_2 and the mirror of the waveform at A_1. According to the previous analysis, the peak current, the valley current, the conduction loss, and the switching loss are the same at a certain switching frequency.

According to the previous analysis, the device loss at certain switching frequency is the same at the four example operating points. As a result, the optimal operating status is also the same. Due to the symmetry, the optimal operating status of any point on the *V–I* plane can be obtained by finding the optimum of the corresponding point in Region *A* I: $\{(v_{\rm ac}, i_{\rm ac})|0 < v_{\rm ac} < V_{\rm bus}/2,\ 0 < i_{\rm ac} < I_{\rm ac,max}\}$, where $I_{\rm ac,max}$ is the peak of the instantaneous output current at full load. It is worth noting that for an *N*-level inverter, the optimization on the whole *V–I* plane can be simplified to the optimization in the region: $\{(v_{\rm ac}, i_{\rm ac})|0 < v_{\rm ac} < 2V_{\rm bus}/(N-1),\ 0 < i_{\rm ac} < I_{\rm ac,max}\}$, which can dramatically simplify the analysis and calculation.

III. Derivation and Curve Fitting of the Optimum

In this section, the objective function is derived first and the device loss model of CCM and DCM in Region *A* I is derived respectively. Although it is not practical to obtain the analytical solution of the optimum, the numerical solution can be obtained. Finally, the optimal solution is fitted with a simple function, which can be easily implemented in the DSP controller.

A. Objective Function

In CCM or DCM operation, the switching frequency is a function of the inductor peak current, i.e., $f_{\rm sw}(i_{\rm pk})$. The objective function Min : $P_{\rm loss}(f_{\rm sw}(i_{\rm pk}))$ can be expressed as

$$\text{Min}: \ P_{\rm loss}\ (i_{\rm pk}) = \ P_{\rm cond}\ (i_{\rm pk}) + P_{\rm sw}\ (i_{\rm pk}) + P_{\rm oss}\ (i_{\rm pk}) \quad (1)$$

where the inductor peak current $i_{\rm pk}$ is the only variable. $P_{\rm cond}$ is the conduction loss of the MOSFETs. $P_{\rm sw}$ is a component of the switching loss which is dependent on the switched current, switched voltage, and gate drive circuit. $P_{\rm oss}$ is the switching loss related to the energy stored in the junction capacitor $C_{\rm oss}$.

B. Loss Model in CCM

In CCM, the objective function should be subject to the restriction

$$\text{S. t.}: i_{\rm ac} < i_{\rm pk} < 2i_{\rm ac} \quad (2)$$

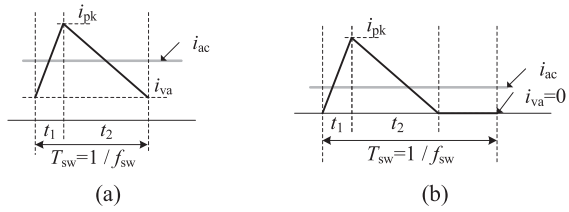

Fig. 6. Inductor waveform and the variables used in the calculation. (a) CCM. (b) DCM.

where $i_{\rm pk}$ is the inductor peak current and $i_{\rm ac}$ is the instantaneous output current. The variables used in the calculation are shown in Fig. 6(a).

The switching frequency, time intervals t_1 and t_2, and inductor valley current $i_{\rm va}$ can be calculated by $i_{\rm pk}$ and the circuit parameters, i.e.,

$$\begin{cases} f_{\rm sw} = \frac{v_{\rm ac}(V_{\rm bus}/2 - v_{\rm ac})}{(i_{\rm pk} - i_{\rm ac})L_{\rm s}V_{\rm bus}} \\ t_1 = \frac{2(i_{\rm pk} - i_{\rm ac})L_{\rm s}}{V_{\rm bus}/2 - v_{\rm ac}} \\ t_2 = \frac{2(i_{\rm pk} - i_{\rm ac})L_{\rm s}}{v_{\rm ac}} \\ i_{\rm va} = 2i_{\rm ac} - i_{\rm pk}\ . \end{cases} \quad (3)$$

In the T-type hybrid-bridge topology, the inductor current flows through three MOSFETs in t_1 and two MOSFETs in t_2. Assume the MOSFETs are all the same, the conduction loss of the inverter can be calculated by

$$P_{\rm cond} = f_{\rm sw}\left(\int_0^{t_1} i_{\rm L}^2 dt \cdot 3R_{\rm dsON} + \int_0^{t_2} i_{\rm L}^2 dt \cdot 2R_{\rm dsON}\right) \quad (4)$$

where $R_{\rm dsON}$ is the ON-state resistance of the MOSFETs.

For the switching loss $P_{\rm sw}$, as the turn-ON and turn-OFF voltages are considered constant, the switching energy can be considered a linear function of the switched current [25] given as

$$P_{\rm sw} = f_{\rm sw}\left(k_{\rm off}i_{\rm pk} + k_{\rm on}i_{\rm va}\right) \quad (5)$$

where $k_{\rm OFF}$ and $k_{\rm ON}$ are constants depending on the dc voltage and the MOSFET switching speed.

$C_{\rm oss}$ related loss includes the discharging loss of the active switch capacitor and the charging loss of the other switch capacitor [26]. In a T-type bridge, three junction capacitors are involved in the charging–discharging process during the hard turn-ON transition. However, for the normally-OFF switch, e.g., S_1 in Region *A* I operation, the drain–source voltage is high and the charging loss can be negligible. Since the switches are considered all the same, $P_{\rm oss}$ can be calculated as

$$P_{\rm oss} = f_{\rm sw}C_{\rm oss,eq}\left(\frac{V_{\rm bus}}{2}\right)^2 \quad (6)$$

where $C_{\rm oss,eq}$ should be the charge-equivalent capacitance according to [27].

C. Loss Model in DCM

In DCM, the inductor peak current is always higher than that in CCM and the restriction is different from CCM as

$$\text{S.t.}: i_{\text{pk}} > 2i_{\text{ac}}\,. \tag{7}$$

The variables f_{sw}, t_1, t_2, and i_{va} shown in Fig. 6(b) can be calculated by

$$\begin{cases} f_{\text{sw}} = \frac{v_{\text{ac}}(V_{\text{bus}}/2 - v_{\text{ac}})i_{\text{ac}}}{(i_{\text{pk}}/2)^2 L_{\text{s}} V_{\text{bus}}} \\ t_1 = \frac{i_{\text{pk}} L_{\text{s}}}{V_{\text{bus}}/2 - v_{\text{ac}}} \\ t_2 = \frac{i_{\text{pk}} L_{\text{s}}}{v_{\text{ac}}} \\ i_{\text{va}} = 0\,. \end{cases} \tag{8}$$

The conduction loss is the same as (4) in CCM while the switching loss only consists of the turn-OFF loss at peak current since $i_{\text{va}} = 0$, which is given by

$$P_{\text{sw}} = f_{\text{sw}} k_{\text{off}} i_{\text{pk}}. \tag{9}$$

In DCM, the drain–source voltage of MOSFETs will oscillate during the dead time zone, and also, P_{oss} will oscillate depending on the turn-ON point. The voltage parasitic oscillation of the active MOSFET is around (V_{bus}/2–v_{ac}) and the amplitude is v_{ac}. Without considering the circuit damping effect, the valley voltage may reach 0 when $v_{\text{ac}} \geq V_{\text{bus}}/4$ and be (V_{bus}/2–2v_{ac}) when $v_{\text{ac}} < V_{\text{bus}}/4$. With proper detection, valley switching can be achieved, and the switching loss can be minimized. For simplicity, P_{oss} is calculated considering valley switching

$$P_{\text{oss}} = \begin{cases} f_{\text{sw}} C_{\text{oss,eq}} \left(\frac{V_{\text{bus}}}{2} - 2v_{\text{ac}}\right)^2, & v_{\text{ac}} < \frac{V_{\text{bus}}}{4} \\ 0, & \frac{V_{\text{bus}}}{4} < v_{\text{ac}} < \frac{V_{\text{bus}}}{2} \end{cases}. \tag{10}$$

D. Optimal Solution and Curve Fitting

Combining the above equations, the numerical solution of the optimal inductor peak current can be obtained. According to the analysis in Section II, the optimum of any point on the *V–I* plane can be obtained by solving the optimum of the corresponding point in Region *A* I, which can dramatically simplify the analysis and calculation. Therefore, the optimal values of (1) are solved in Region *A* I, i.e., $\{(v_{\text{ac}}, i_{\text{ac}})|0 < v_{\text{ac}} < V_{\text{bus}}/2,\ 0 < i_{\text{ac}} < I_{\text{ac,max}}\}$. In this work, considering the bus voltage is 400 V and the output power is 1 kW, Region *A* I can be expressed as: $\{(v_{\text{ac}}, i_{\text{ac}})|0 < v_{\text{ac}} < 200\text{V},\ 0 < i_{\text{ac}} < 6.42\text{A}\}$. The circuit parameters for 1 kW prototype are used in the calculation and listed in Table I. Once the circuit parameters are determined, the optimal inductor peak current is only related to the instantaneous output current i_{ac} and output voltage v_{ac}. The calculated optimal inductor peak current surface $i_{\text{pk,cal}}(v_{\text{ac}}, i_{\text{ac}})$ with parameters given in Table I is plotted in Fig. 7, where the BCM surface is plotted and the optimal operating modes are labeled. When $i_{\text{pk,cal}} = 2i_{\text{ac}}$, the inverter is expected to operate in BCM. When $i_{\text{pk,cal}} > 2i_{\text{ac}}$, the inverter will operate in DCM, and when $i_{\text{pk,cal}} < 2i_{\text{ac}}$, the inverter will operate in CCM.

Fig. 8 shows the normalized calculated optimal inductor peak current $i_{\text{pk,cal}}/I_{\text{ac,max}}$ versus normalized output current

TABLE I
CIRCUIT PARAMETERS

Parameters	Value
Input DC bus voltage, V_{bus}	400 V
Output AC voltage, $V_{\text{ac,rms}}$	220 V
Rated output power, P_{o}	1 kW
Power factor range, PF	0.9—1
Switching frequency range	25kHz—100 kHz
Inductor peak current limit, $I_{\text{pk,lim}}$	7.88A
MOSFETs Part No.	IPW60R070CFD7
On-state resistance of MOSFETs, R_{dsON}	57 mΩ
Constant of turn-on loss, k_{ON}	8.37e-6
Constant of turn-off loss, k_{OFF}	2.91e-6
Charge-equivalent capacitance, $C_{\text{oss,eq}}$	788 pF
Inverter-side inductor, L_{s}	170 μH
Grid-side inductor, L_{g}	500 μH
Filter capacitor, C_{g}	2 μF
MCU Part No.	TMS320F28377S
Current sensor Part No.	ACS730-20AB-T

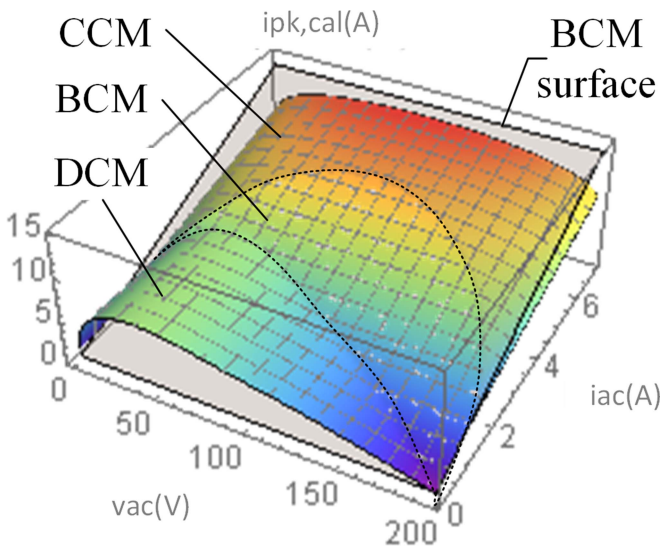

Fig. 7. Calculated optimal inductor peak current surface $i_{\text{pk,cal}}(v_{\text{ac}}, i_{\text{ac}})$ based on the 1-kW prototype.

$i_{\text{ac}}/I_{\text{ac,max}}$ when v_{ac} is fixed as 20 V, 100 V, and 160 V, i.e., the normalized output voltage $v_{\text{ac}}/V_{\text{bus}}$ is 0.05, 0.25, and 0.4 respectively. When the output current i_{ac} is low, $i_{\text{pk,cal}}$ is independent of i_{ac} and the inverter will operate in DCM since $i_{\text{pk,cal}} > 2i_{\text{ac}}$. The optimal switching frequency and switching loss will decrease as i_{ac} decreases since $i_{\text{pk,cal}}$ remains constant. As i_{ac} increase, the optimal solution is on the boundary, which suggests the inverter will operate in BCM. When i_{ac} is high, $i_{\text{pk,cal}}$ is nearly linear about i_{ac}, and the inverter will operate in CCM to decrease the conduction loss.

It is worth noting that the curves are not coinciding at different v_{ac}. The optimized peak current varies not only with i_{ac} but also with v_{ac}. Also, the current thresholds for operation modes transition are not a monotonic function of v_{ac}, as shown in Fig. 10. The reason is that the switching frequency is not a monotonic function of v_{ac} according to (3).

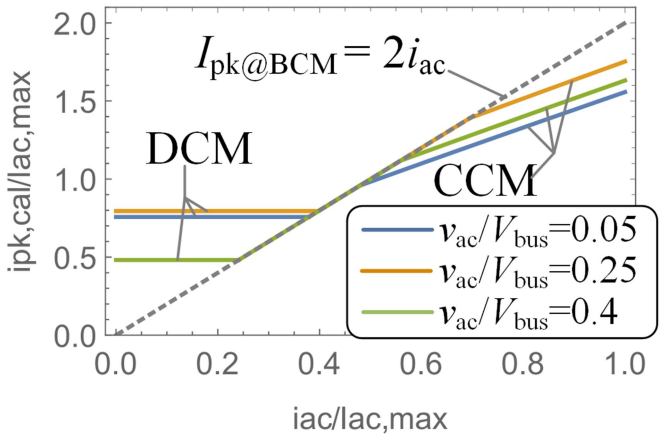

Fig. 8. Normalized calculated optimal inductor peak current $i_{pk,cal}/I_{ac,max}$ as functions of the normalized output current $i_{ac}/I_{ac,max}$.

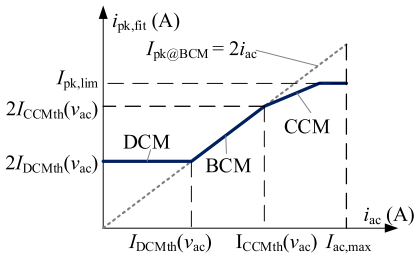

Fig. 9. Diagram of the designed optimal inductor peak current $i_{pk,fit}$.

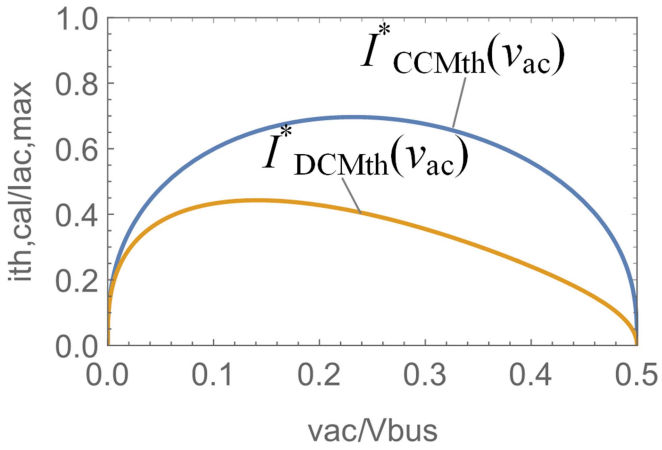

Fig. 10. Normalized curves of the current thresholds as functions of the normalized output voltage v_{ac}/V_{bus}.

According to Fig. 8, the optimal inductor peak current fitting function $i_{pk,fit}$ can be designed as a piecewise linear function of i_{ac} as (11). The diagram of $i_{pk,fit}$ is shown in Fig. 9. The threshold current from DCM to BCM and the threshold from BCM to CCM are expressed as $I_{DCMth}(v_{ac})$ and $I_{CCMth}(v_{ac})$, respectively, which are functions of the output voltage v_{ac}. The slope of $i_{pk,fit}$ in CCM a_1 is a constant which can be obtained by curve fitting. Considering the inductor saturation, a current limitation $I_{pk,lim}$ lower than the inductor saturation current should

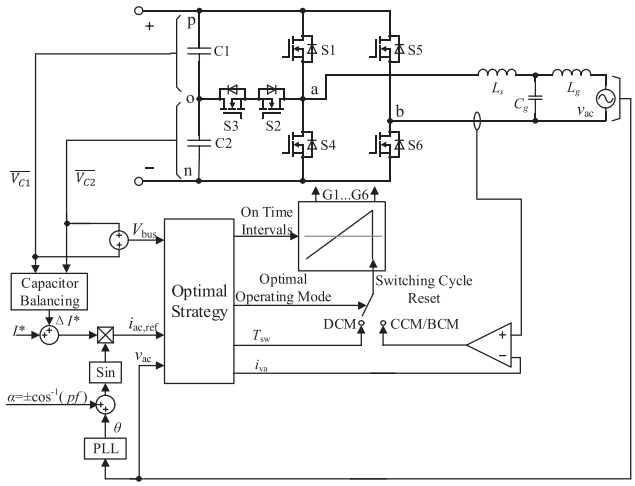

Fig. 11. Control diagram for the proposed VSF multimode scheme.

be set.

$$i_{pk,fit}\ (v_{ac}, i_{ac}) = \begin{cases} 2I_{DCMth}, & i_{ac} < I_{DCMth} \\ 2i_{ac}, & I_{DCMth} \le i_{ac} < I_{CCMth} \\ a_1\,(i_{ac} - I_{CCMth}) + 2I_{CCMth}, & I_{CCMth} \le i_{ac} \&\& i_{pk,fit} \le I_{pk,lim} \\ I_{pk,lim}, & i_{pk,fit} > I_{pk,lim} \end{cases}. \tag{11}$$

Fig. 10 shows the normalized function of $I_{DCMth}(v_{ac})$ and $I_{CCMth}(v_{ac})$. The normalized threshold is defined as $I^*_{DCMth}(v_{ac}) = I_{DCMth}(v_{ac})/I_{ac,max}$ and $I^*_{CCMth}(v_{ac}) = I_{CCMth}(v_{ac})/I_{ac,max}$. As shown in Fig. 10, I_{DCMth} and I_{CCMth} are zero at $v_{ac} = 0$ and $v_{ac} = V_{bus}/2$, and both I_{DCMth} and I_{CCMth} can be fitted by the following function:

$$I_{th,fit} = \frac{(1/2 - k_{vac})\,k_{vac}}{k_0 + k_1 k_{vac} + k_2 k_{vac}^2} \tag{12}$$

where k_0, k_1, and k_2 are the curve-fitting coefficients, and

$$k_{vac} = \begin{cases} v_{ac}/V_{bus}, & v_{ac} < V_{bus}/2 \\ 1 - v_{ac}/V_{bus}, & v_{ac} \ge V_{bus}/2 \end{cases}. \tag{13}$$

Since the circuit parameters are determined, the fitting coefficients a_1, k_0, k_1, and k_2 can be calculated offline. As a result, the optimal inductor peak current can be calculated by the polynomial fractions in (11), (12), and (13) in the DSP controller.

IV. Control System Implementation

A. Control Method

Fig. 11 shows the control diagram of the prototype. The hybrid current control method is used to control inductor current in CCM and BCM [20], [28]. The first interval t_1 is calculated by the DSP and the switching cycle ends when the inductor current reaches the preset boundary i_{va}. For DCM operation, the time intervals are predicted by the required average current $i_{ac,ref}$, the input voltage V_{bus}, and the instant output voltage v_{ac}.

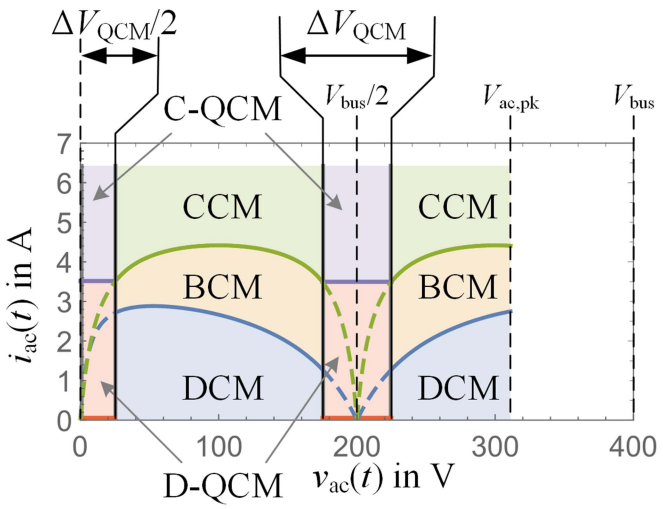

Fig. 12. Optimal operating mode on Quadrant I of the *V–I* plane.

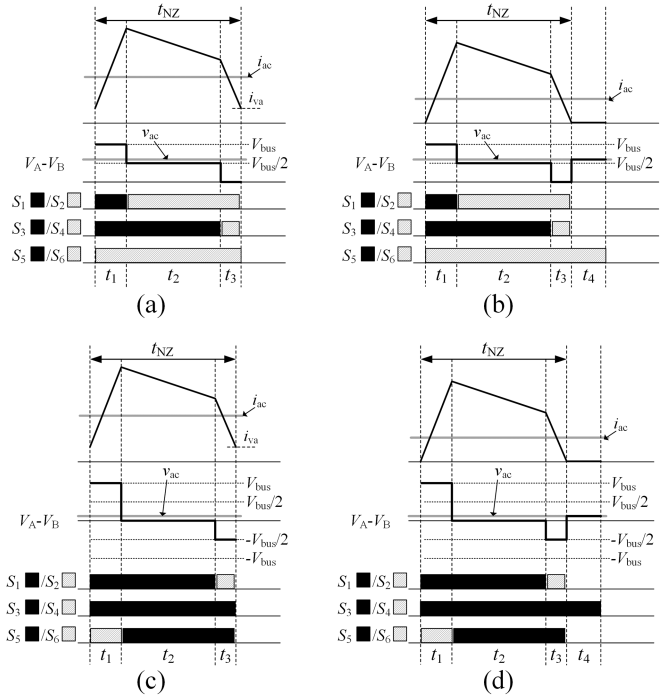

Fig. 13. Inductor current waveform and switching sequence of (a) C-QCM in the region near $v_{ac} = V_{bus}/2$, (b) D-QCM in the region near $v_{ac} = V_{bus}/2$, (c) C-QCM in the region near $v_{ac} = 0$, (d) D-QCM in the region near $v_{ac} = 0$.

The switching cycle ends with the calculated switching period T_{sw}. The optimal operating mode is determined to choose which signal is used to reset the switching cycle. The optimal strategy is not calculated in each switching cycle; it is calculated in a slow interrupt period, i.e., 40 μs in the experiment. The optimal operating mode and the control variables are updated by each interrupt period.

A conventional capacitor voltage balancing control is also adopted in the control scheme. The average voltages of the bus divided capacitors during a line cycle are measured, which is referred as $\overline{V_{C1}}$ and $\overline{V_{C2}}$, respectively. In the voltage balancing control, these two average voltages are compared and the error will be used to offset the current reference to balance the capacitor voltages. It has been widely reported and used in real applications, so it is not elaborated here.

In unipolar pulsewidth modulation control of the conventional H-bridge grid-tied inverters, current distortion may occur near the voltage-zero-crossing region due to dead time or limited duty cycle [29]. In the T-type hybrid-bridge inverter, similar current distortion may also occur when the output voltage v_{ac} is near half bus voltage $V_{bus}/2$. To solve this problem, the authors have proposed quadrilateral current mode (QCM), or so-called trapezium conduction mode, in which the inductor current is shaped like a quadrilateral [28], [30]. In this article, QCM is adopted near the region of $v_{ac} = 0$ or $|v_{ac}| = V_{bus}/2$. The detailed principle and implementation of QCM are expressed as follows.

B. Principle and Implementation of QCM

Fig. 12 shows the operating modes on the first quadrant of *V–I* plane with QCM implementation. The QCM operation consists of continuous-QCM (C-QCM) and discontinuous-QCM (D-QCM). As shown in Fig. 12, C-QCM is inserted between CCM or BCM, whereas D-QCM is inserted between DCM operations. Take a point near $v_{ac} = V_{bus}/2$ as an example. When the output current is high, the inverter will operate in C-QCM as shown in Fig. 13(a) where the inductor current waveform is continuous. The differential voltage between the two switching legs V_A–V_B switches among V_{bus}, $V_{bus}/2$, and 0 in sequence. As the output current decreases, the inverter will operate in D-QCM as shown in Fig. 13(b). In D-QCM, there is a dead time zone t_4 where the inductor current is zero. The inductor current waveforms and switching sequence of C-QCM and D-QCM in the region near $v_{ac} = 0$ are shown in Fig. 13(c) and (d). In the region near $v_{ac} = 0$, the differential voltage between the two switching legs V_A–V_B switches among V_{bus}, 0, and $-V_{bus}/2$ in sequence.

In QCM operation, the duty cycle of the second interval is chosen as a control variable and defined as

$$d_M = t_2 / (t_1 + t_2 + t_3) = t_2 / t_{NZ} \tag{14}$$

where t_{NZ} is the time interval when the inductor current is not zero as shown in Fig. 13.

As shown in Fig. 14, d_M determines the shape of the quadrilateral. When $d_M = 0$, the middle time interval t_2 is bypassed and the inverter will operate as a conventional H-bridge inverter. When d_M is maximum, either t_1 or t_3 is bypassed according to the output voltage v_{ac} and the inverter will operate in three-level TCM. The maximum $d_{M,max}$ can be calculated by (15). When d_M is between 0 and $d_{M,max}$, the shape of the inductor current is a quadrilateral.

$$d_{M,max} = \begin{cases} 2 \cdot \mathrm{Min}\left(v_{ac}, V_{bus} - v_{ac}\right) / V_{bus}, & \text{Region near half bus voltage} \\ \mathrm{Min}\left(\frac{V_{bus}+2v_{ac}}{V_{bus}}, \frac{V_{bus}-v_{ac}}{V_{bus}}\right), & \text{Region near zero} - \text{crossing} \end{cases}. \tag{15}$$

TABLE II
CALCULATION FORMULAS OF QCM

	Region near half-bus voltage		Region near zero-crossing	
	C-QCM	D-QCM	C-QCM	D-QCM
T_{sw}	$\frac{8(i_{ac}-i_{va})L_sV_{bus}}{4(V_{bus}-v_{ac})v_{ac}-d_M^2V_{bus}^2}$	$\frac{i_{pk,ref}^2L_sV_{bus}}{i_{ac}(V_{bus}-\Delta V_{QCM})\Delta V_{QCM}}$	$\frac{6(i_{ac}-i_{va})L_sV_{bus}}{(V_{bus}-v_{ac})(V_{bus}+2v_{ac})-d_M^2V_{bus}^2}$	$\frac{i_{pk,ref}^2L_sV_{bus}}{i_{ac}(V_{bus}-\Delta V_{QCM})\Delta V_{QCM}}$
t_{NZ}	T_{sw}	$\sqrt{\frac{8i_{ac}L_sV_{bus}T_{sw}}{4(V_{bus}-v_{ac})v_{ac}-d_M^2V_{bus}^2}}$	T_{sw}	$\sqrt{\frac{6i_{ac}L_sV_{bus}T_{sw}}{((V_{bus}-v_{ac})(V_{bus}+2v_{ac})-d_M^2V_{bus}^2)}}$
t_1	$\left(\frac{v_{ac}}{V_{bus}}-\frac{d_M}{2}\right)t_{NZ}$		$\left(\frac{V_{bus}+2v_{ac}}{3V_{bus}}-\frac{d_M}{3}\right)t_{NZ}$	
t_2	d_Mt_{NZ}		d_Mt_{NZ}	
t_3	$\left(\frac{V_{bus}-v_{ac}}{V_{bus}}-\frac{d_M}{2}\right)t_{NZ}$		$\left(\frac{2(V_{bus}-v_{ac})}{3V_{bus}}-\frac{2d_M}{3}\right)t_{NZ}$	
t_4	0	$T_{sw}-t_{NZ}$	0	$T_{sw}-t_{NZ}$

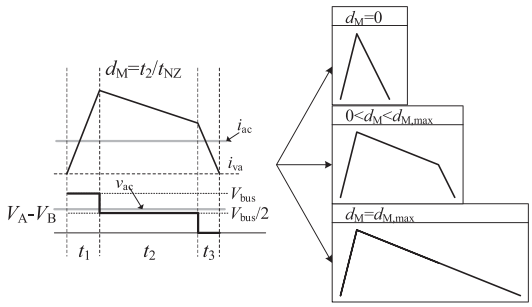

Fig. 14. Inductor current waveform and effect of d_M in QCM.

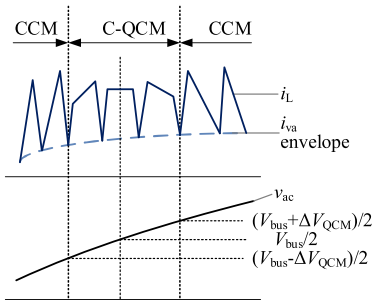

Fig. 15. Inductor current and the instantaneous output voltage during CCM-CQCM-CCM transition.

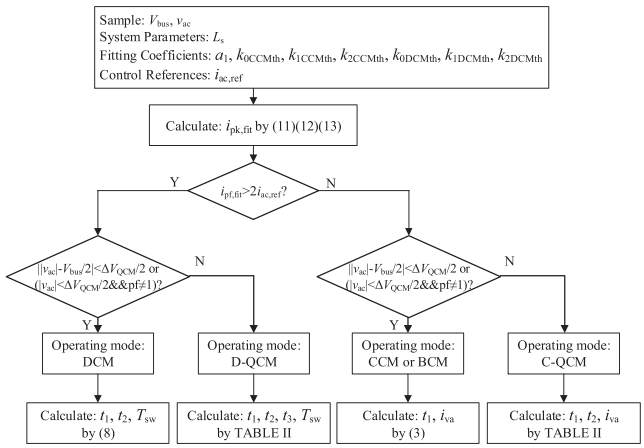

Fig. 16. Flowchart of the optimal strategy.

To achieve high efficiency, d_M should be as large as possible. However, d_M cannot be too large due to the lower limit of t_1 and t_3 intervals [28]. Thus, the design of d_M is recommended as 0.6–0.8$d_{M,max}$.

An example of CCM to C-QCM transition near half bus voltage is shown in Fig. 15. The inverter will operate in C-QCM when $(V_{bus}-\Delta V_{QCM})/2 < v_{ac} < (V_{bus}+\Delta V_{QCM})/2$, otherwise it will operate in CCM. ΔV_{QCM} is the width of QCM. To ensure current quality, the envelope of inductor valley current i_{va} should be continuous at the transition between CCM and C-QCM. The inductor valley current in C-QCM is designed by the following equation:

$$i_{va} = 2i_{ac} - i_{pk,fit}\big|_{v_{ac}=(V_{bus}-\Delta V_{QCM})/2}. \tag{16}$$

In C-QCM, the switching period and time intervals can be calculated using the control variables i_{va} and d_M. In D-QCM, i_{va} is always zero. To smooth the output current, the switching frequency in D-QCM is designed equal to the switching frequency of DCM at the transition point. The expressions of the switching period and time intervals in QCM are summarized in Table II.

The flowchart of the optimal control strategy is shown in Fig. 16. The inductor peak current reference $i_{pk,fit}$ is calculated by (11), (12), and (13) first. Then, it is compared with $2i_{ac,ref}$ to determine whether the operating mode is continuous or discontinuous. Next, the sampled output voltage v_{ac} is used to determine whether the inductor current waveform should be triangular or quadrilateral. Finally, the control variables of the corresponding operating mode are calculated.

V. SIMULATION RESULTS

To demonstrate the proposed VSF multimode control scheme, simulations are executed in various conditions using the parameters in Table I. The simulation software used is PLECS and the control scheme is implemented by the C-Script block.

The state-plane trajectory and simulation waveforms of the proposed control strategy in unity and nonunity PF operations are shown in Figs. 17 and 18, respectively. Since the output current i_{ac} is small near $v_{ac} = 0$ in unity PF operation, QCM

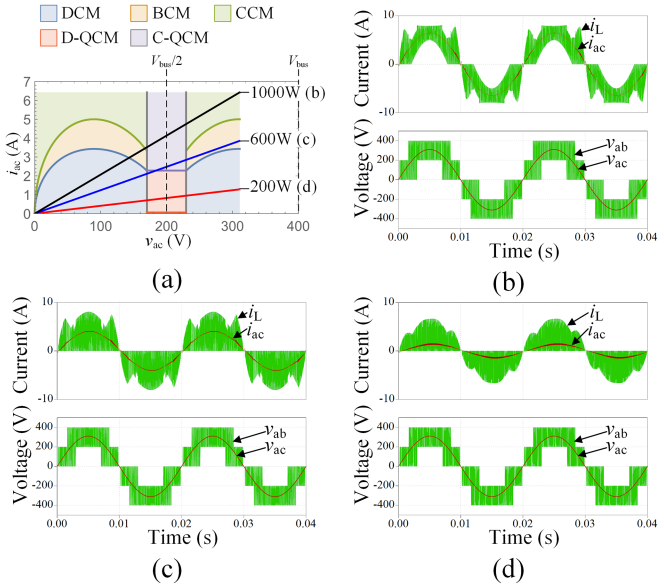

Fig. 17. (a) Optimal operating mode and state-plane trajectory on Quadrant I of the *V–I* plane in unity PF operation and simulation waveforms at (b) 1000 W, (c) 600 W, and (d) 200 W. Condition: PF = 1.

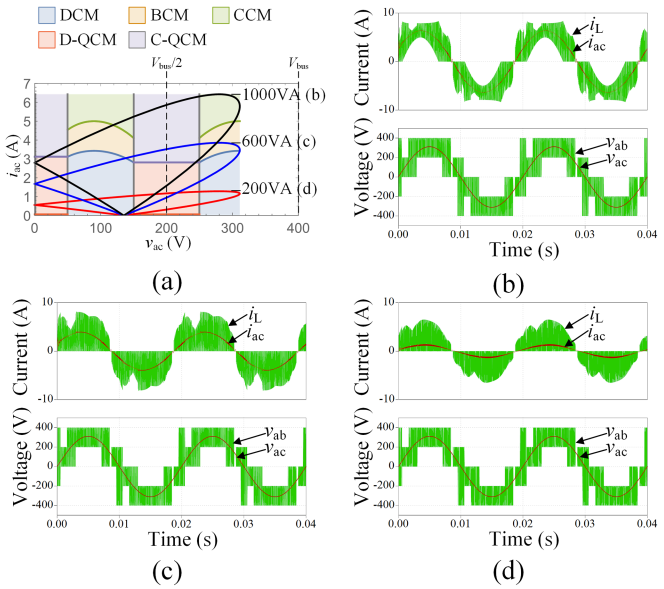

Fig. 18. (a) Optimal operating mode and state-plane trajectory on Quadrant I of the *V–I* plane in nonunity PF operation and simulation waveforms at (b) 1000 VA, (c) 600 VA, and (d) 200 VA. Condition: PF = 0.9, current leading.

near $v_{ac} = 0$ is unnecessary. Otherwise, QCM is used near $v_{ac} = 0$ in nonunity PF operation.

As shown in Fig. 17(a), the black line represents the full load operation at PF = 1. The inverter will operate in CCM when the instantaneous power is high. As the instantaneous power decreases, the inverter will operate in C-QCM or BCM automatically and finally operate in DCM. In medium load, e.g. the blue line in Fig. 17(a), the inverter will operate in BCM at the peak of the instantaneous power. In light load as the red line in Fig. 17(a), the inverter will operate in DCM or D-QCM during

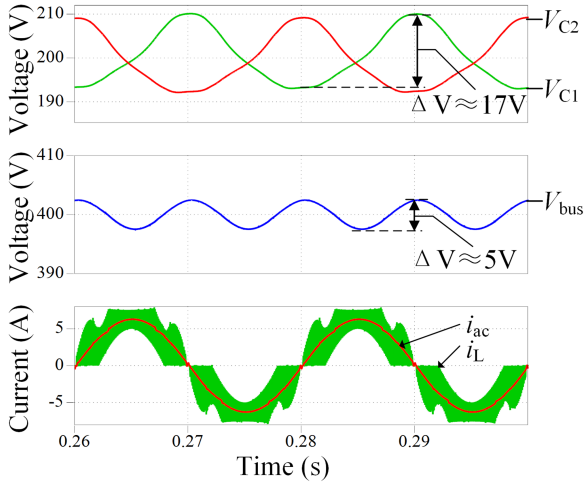

Fig. 19. Simulated line frequency ripple of the DC capacitor and the DC bus, $P_o = 1$ kW, PF = 1.

the whole line cycle. The corresponding simulation waveforms in the unity PF operation are shown in Fig. 17(b)–(d).

Similarly, in nonunity PF operation, the trajectories of three cases are shown in Fig. 18(a). The inverter will operate in both continuous and discontinuous operating modes in heavy load while only operating in a discontinuous operating mode in light load. The corresponding simulation waveforms in nonunity PF operation are shown in Fig. 18(b)–(d).

The key waveform of capacitor voltage balancing is shown in Fig. 19. The line frequency ripple is filtered by the dc-link capacitors as in a conventional single-phase voltage source inverter. As shown in Fig. 19, the twice-line-frequency ripple voltage is only 5 V, which is quite small compared to the bus voltage. The line frequency ripple voltage of the two capacitors is about 17 V. The average voltages of the two capacitors are around 200 V, and they are well balanced with the voltage balancing control.

The power losses of the conventional CSF scheme and the proposed VSF multimode control scheme are estimated and compared using the parameters given in Table I, including $P_{\rm cond}$, $P_{\rm sw}$, and $P_{\rm oss}$. To make the comparison more reasonable, the inductor peak current limit $I_{\rm pk,limit}$ is the same in CSF and VSF methods. Since $I_{\rm pk,limit}$ is 7.88 A, the switching frequency is 100 kHz in CSF and varies within 25–100 kHz in VSF control. The results are shown in Fig. 20. The device loss is reduced greatly by using the proposed optimal VSF scheme, especially in light load. Even though power loss in QCM operation is slightly higher, the proposed scheme can save total power loss in the whole load range.

Fig. 21 shows the ripple of the output current i_{ac} in the simulation. The total harmonic distortion (THD) is also shown in Fig. 21. For the conventional CSF control scheme, the output current ripple is large when the output voltage is around $V_{\rm bus}/2$. The VSF control will reduce the ripple peaks near $V_{\rm bus}/2$ due to the adoption of QCM and thus the THD is improved at the 1-kW output condition. However, the THD with VSF control will be higher than that with CSF control when output power

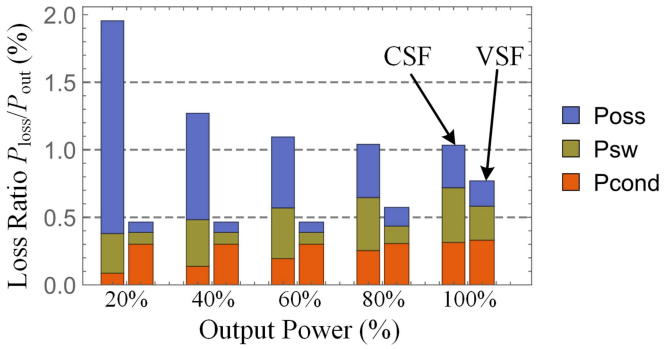

Fig. 20. Device loss distribution of CSF control and proposed VSF control at different output power.

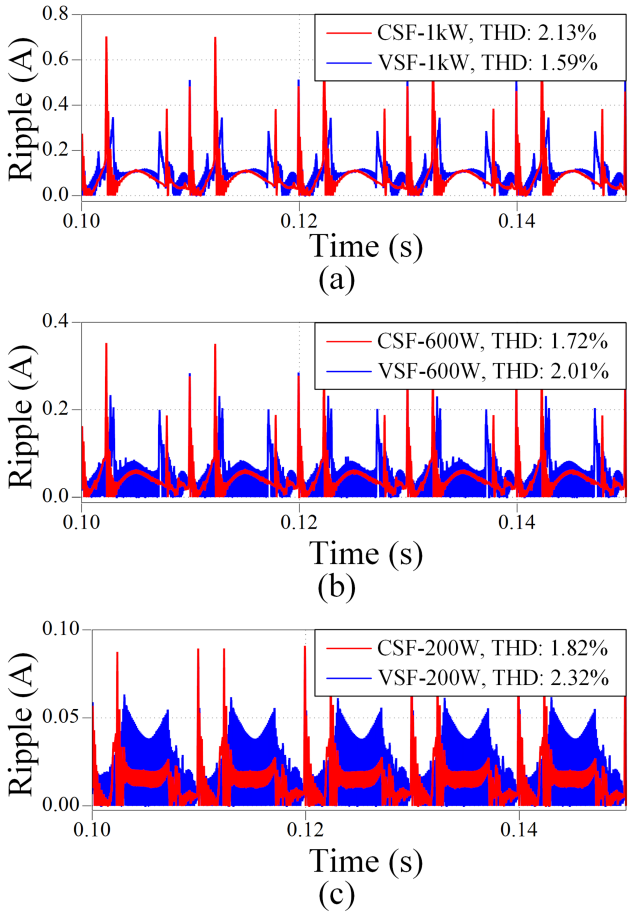

Fig. 21. Output current ripple and THD in the simulation at (a) 1 kW, PF = 1, (b) 600 W, PF = 1, and (c) 200 W, PF = 1.

decreases due to the decreasing switching frequency. To meet the THD requirements of the grid, it is recommended to set a lower bound for the switching frequency. As the study in [31] suggests, the minimum switching frequency should be higher than twice the *LCL* filter resonant frequency.

VI. Experimental Validation

A 1-kW T-type hybrid-bridge inverter prototype is built as shown in Fig. 22. The power stage design is the same as that for

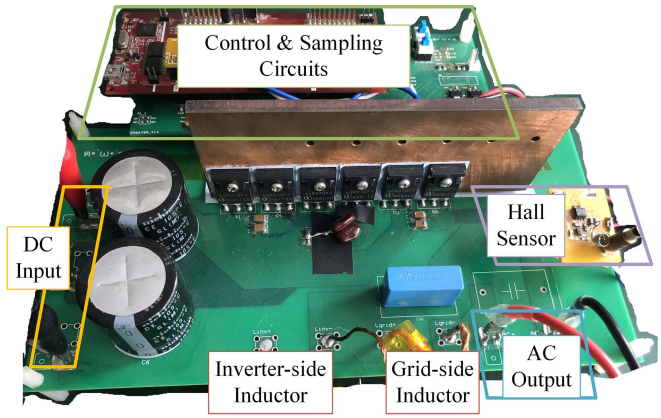

Fig. 22. 1-kW T-type hybrid-bridge five-level inverter prototype.

a conventional inverter with a CSF control method. The inductor is usually designed based on the ripple current at maximum output power. The circuit parameters are also listed in Table I. A DSP TMS320F28377S is used as a digital controller with a 200 MHz system clock. A 25-kHz interrupt frequency is used to implement the proposed VSF control scheme. A dc voltage source is connected to the input port to provide a constant voltage dc bus. For safety considerations, the output port is connected to an ac voltage source in parallel with a resistive load to emulate the grid.

The experimental waveforms are shown in Figs. 23 and 24. In full load and unity PF condition, as shown in Fig. 24(a), the inverter operated in CCM with high switching frequency at high instantaneous power and DCM with low switching frequency at low instantaneous power. Besides, C-QCM is used and the zoom-in waveform shows that the inductor valley current is continuous at the transition between C-QCM and CCM. Fig. 24(b) shows that the inverter operated in BCM at peak power in a line cycle in medium load (600 W), which is consistent with the previous analysis shown in Fig. 17(a). In Fig. 24(c), the inverter operated in DCM and D-QCM in the whole line cycle in light load. The zoom-in waveform shows the transition from D-QCM to DCM. In Fig. 24(d), the inverter operated in full load and nonunity PF condition. As shown in the zoom-in waveform, the inverter operated in DCM when the output current is positive and the output voltage is negative. Then, the inverter ran into D-QCM when the output voltage is near zero-crossing. As the instantaneous output voltage increases, the inverter operated in CCM again.

The efficiency of the proposed optimal VSF scheme is shown in Fig. 25. The conventional CSF scheme is also implemented on the same prototype to make a reasonable comparison. The results show that the proposed VSF scheme can improve efficiency, especially in light to medium loads. In nonunity PF operation, the addition of QCM will slightly decrease the efficiency. However, the efficiency of the VSF scheme is still higher than that of the CSF scheme over a wide power range. The weighted average efficiency according to CEC and EU efficiency is calculated and summarized in Table III. Compared with the CSF scheme, the proposed VSF scheme can improve the weighted efficiency by

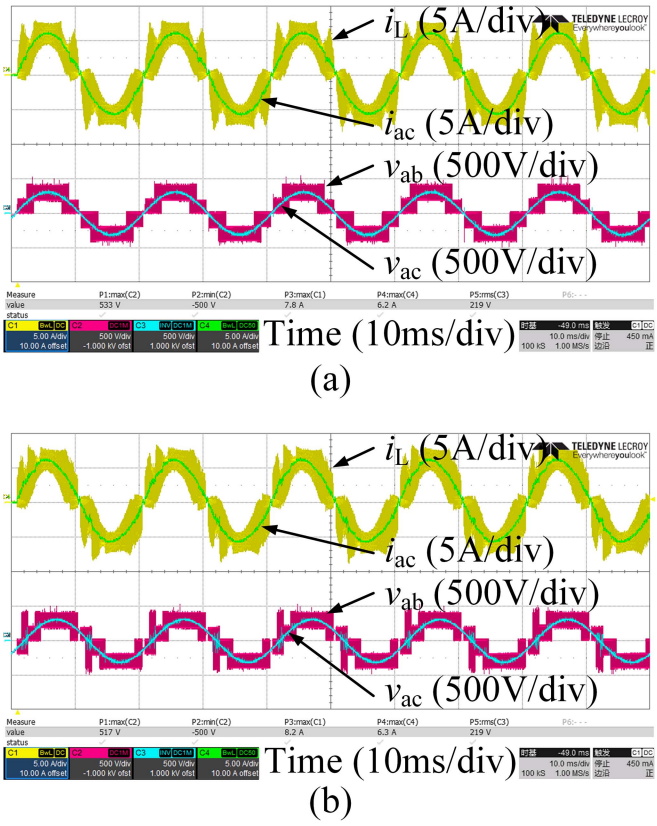

Fig. 23. Experimental waveforms at (a) 1 kW, PF = 1 and (b) 1 kVA, PF = 0.9, current leading.

TABLE III
PERFORMANCE COMPARISON BETWEEN CSF SCHEME AND THE PROPOSED VSF MULTIMODE SCHEME

	CSF, *PF*=1	VSF, *PF*=1	CSF, *PF*=0.9	VSF, *PF*=0.9
CEC efficiency	97.52%	98.50%	97.31%	97.94%
EU efficiency	97.14%	98.44%	97.04%	97.66%
THD (Rated Power)	5.092%	4.791%	8.150%	4.945%

about 1% in unity PF operations and about 0.6% in nonunity PF operations.

The THD at rated power (1 kW) is measured and shown in Table III. In the CSF scheme, the THD is poor due to the current distortion near voltage zero-crossing and $V_{bus}/2$. The reason is that the CSF scheme employs the same control method as the VSF scheme for simplicity, which does not sample the average inductor current and differs from the conventional PI control. When the output voltage approaches 0 or $V_{bus}/2$, the switches will not turn ON because the duty cycle is smaller than the dead time (400 ns in the prototype), leading to current distortion. The THD is even worse in nonunity operation because current distortion is more severe both at $v_{ac} = 0$ and $V_{bus}/2$ since the current amplitude is larger.

For the proposed VSF scheme, current distortion near zero-crossing and $V_{bus}/2$ is mitigated due to QCM operation, and thus the THD is slightly improved. The harmonic spectrum of

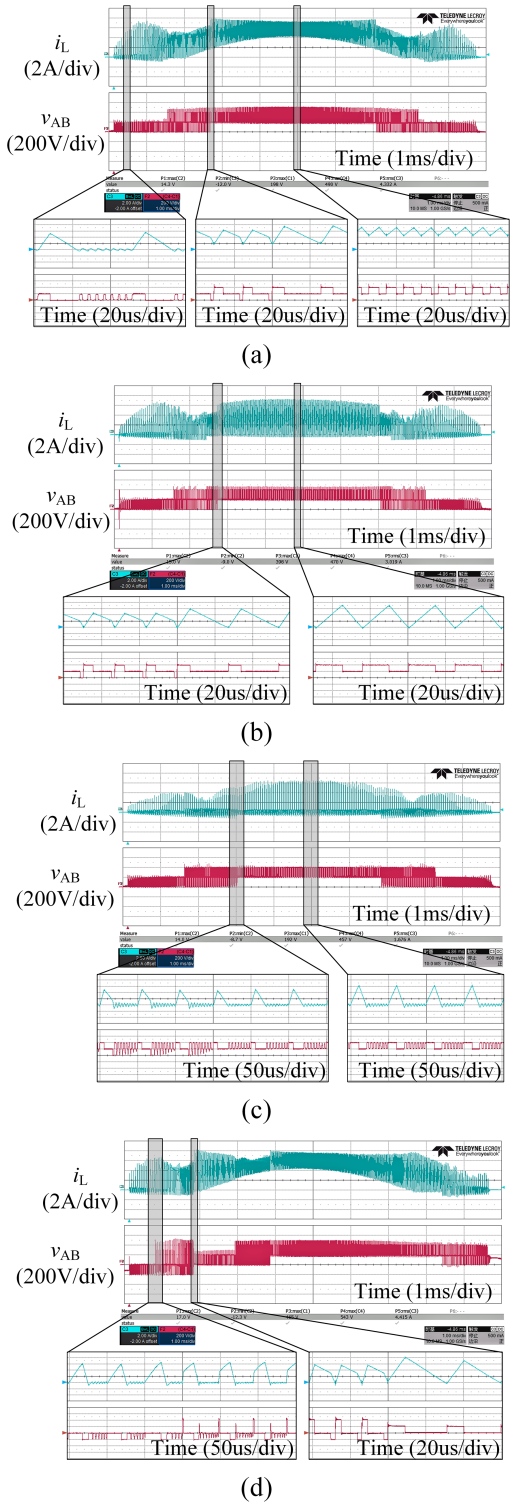

Fig. 24. Experimental waveforms in half-line cycle at (a) 1 kW, PF = 1, (b) 600 W, PF = 1, (c) 200 W, PF = 1, and (d) 1 kVA, PF = 0.9, current leading.

VSF control is shown in Fig. 26. There are several factors that contribute to harmonics in different frequency ranges. Since the inductor current is controlled by the calculated on-time and the valley inductor current, the turn-ON delay, dead time, and sampling errors can lead to inaccurate current tracking,

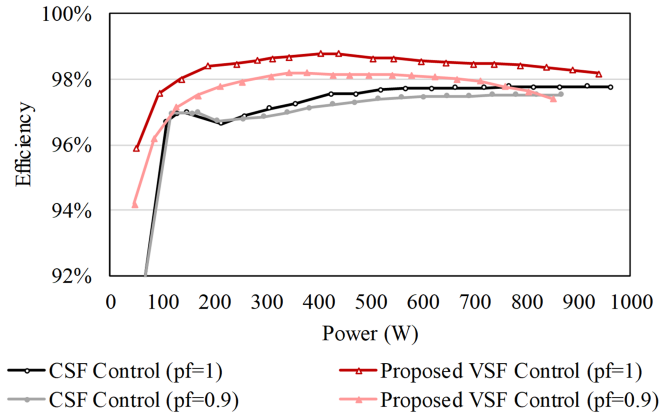

Fig. 25. Measured efficiency comparison between conventional CSF control and proposed VSF control.

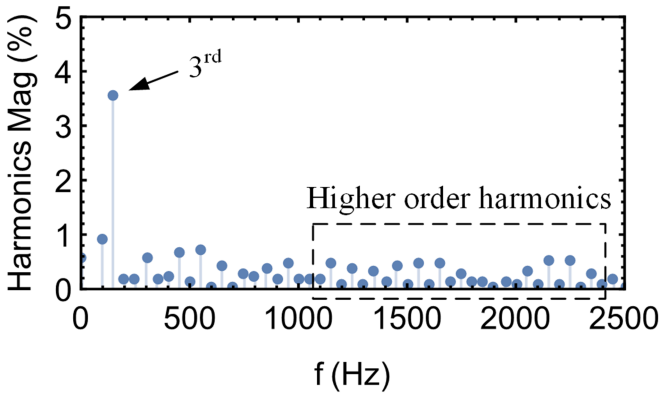

Fig. 26. Harmonic spectrum of the output current with VSF control at 1 kW, PF = 1.

which are the main factors of lower-order harmonics (mainly the third-order harmonic). Meanwhile, higher-order harmonics (mainly above the 20th order) are caused by oscillations under DCM operation due to nonuniform turn-ON [32]. Furthermore, THD improvement can still be expected using approaches like third harmonic injection, suitable compensation, and valley-lock method during DCM operation.

VII. Conclusion

This article proposed a VSF multimode control method for single-phase multilevel inverters in both unity and nonunity PF operation. First, this article demonstrates that the operating points of the inverter in the entire *V–I* plane can be mapped into a small region $A\,\mathrm{I}: \{(v_{\mathrm{ac}}, i_{\mathrm{ac}})|0 < v_{\mathrm{ac}} < V_{\mathrm{bus}}/2,\ 0 < i_{\mathrm{ac}} < I_{\mathrm{ac,max}}\}$ in Quadrant I, which dramatically simplifies the loss analysis. Therefore, the optimal operating mode and switching frequency of all operating points in the *V–I* plane can be derived simply by obtaining the optimal solution in Region *A* I. The optimization is conducted to minimize the power loss of the switches including the conduction loss, switching loss, and C_{oss} loss, which are usually the dominant power losses of the inverter. A VSF multimode strategy is proposed to optimize the loss components since the instantaneous output power always changes in a line cycle. To avoid the current distortion caused by minimum duty cycle limitation, the transition mode QCM has adopted near the zero-crossing point and half bus voltage in this work. The design consideration of the QCM is discussed considering the smooth transition and the saving of power loss. Finally, a T-type hybrid-bridge five-level inverter prototype is built to verify the proposed scheme. Simulation and experiments show the effectiveness of the proposed VSF multimode scheme. Compared with conventional CSF control, the proposed VSF scheme can optimize efficiency over a wide power range. The weighted average efficiency of the proposed VSF control is improved about 1% in unity PF operation and about 0.6% in nonunity PF operation.

References

[1] K. Alluhaybi, I. Batarseh, and H. Hu, "Comprehensive review and comparison of single-phase grid-tied photovoltaic microinverters," *IEEE J. Emerg. Sel. Topics Power Electron.*, vol. 8, no. 2, pp. 1310–1329, Jun. 2020, doi: 10.1109/JESTPE.2019.2900413.

[2] S. Kouro, J. I. Leon, D. Vinnikov, and L. G. Franquelo, "Grid-connected photovoltaic systems: An overview of recent research and emerging PV converter technology," *IEEE Ind. Electron. Mag.*, vol. 9, no. 1, pp. 47–61, Mar. 2015, doi: 10.1109/MIE.2014.2376976.

[3] S.-Y. Park, C.-L. Chen, J.-S. Lai, and S.-R. Moon, "Admittance compensation in current loop control for a grid-tie LCL fuel cell inverter," *IEEE Trans. Power Electron.*, vol. 23, no. 4, pp. 1716–1723, Jul. 2008, doi: 10.1109/TPEL.2008.924828.

[4] Z. J. Zhou, X. Zhang, P. Xu, and W. X. Shen, "Single-phase uninterruptible power supply based on Z-source inverter," *IEEE Trans. Ind. Electron.*, vol. 55, no. 8, pp. 2997–3004, Aug. 2008, doi: 10.1109/TIE.2008.924202.

[5] S. Krauter and J. Bendfeld, "Comparison of microinverters: Update on conversion efficiencies and energy yields," in *Proc. 47th IEEE Photovolt. Spec. Conf.*, 2020, pp. 1429–1432, doi: 10.1109/PVSC45281.2020.9300953.

[6] R. Fernandes and O. Trescases, "A multimode 1-MHz PFC front end with digital peak current modulation," *IEEE Trans. Power Electron.*, vol. 31, no. 8, pp. 5694–5708, Aug. 2016.

[7] C. Wang, S. Xu, X. Fan, S. Lu, and W. Sun, "Novel digital control method for improving dynamic responses of multimode primary-side regulation flyback converter," *IEEE Trans. Power Electron.*, vol. 32, no. 2, pp. 1457–1468, Feb. 2017.

[8] G. C. Christidis, A. C. Nanakos, and E. C. Tatakis, "Hybrid discontinuous/boundary conduction mode of flyback microinverter for AC–PV modules," *IEEE Trans. Power Electron.*, vol. 31, no. 6, pp. 4195–4205, Jun. 2016, doi: 10.1109/TPEL.2015.2470094.

[9] Z. Zhang, M. Chen, W. Chen, C. Jiang, and Z. Qian, "Analysis and implementation of phase synchronization control strategies for BCM interleaved flyback microinverters," *IEEE Trans. Power Electron.*, vol. 29, no. 11, pp. 5921–5932, Nov. 2014, doi: 10.1109/TPEL.2014.2300483.

[10] T. Liu, C. Chen, K. Xu, Y. Zhang, and Y. Kang, "GaN-based megahertz single-phase inverter with a hybrid TCM control method for high efficiency and high-power density," *IEEE Trans. Power Electron.*, vol. 36, no. 6, pp. 6797–6813, Jun. 2021, doi: 10.1109/TPEL.2020.3039386.

[11] J. Chen, D. Sha, and J. Zhang, "Current ripple prediction and DPWM-based variable switching frequency control for full ZVS range three-phase inverter," *IEEE Trans. Ind. Electron.*, vol. 68, no. 2, pp. 1412–1422, Feb. 2021, doi: 10.1109/TIE.2020.2967741.

[12] X. Zhu et al., "A passive variable switching frequency SPWM concept and analysis for DCAC converter," *IEEE Trans. Power Electron.*, vol. 37, no. 5, pp. 5524–5534, May 2022, doi: 10.1109/TPEL.2021.3123190.

[13] Z. Zhang, J. Zhang, and S. Shao, "A variable off-time control method for a single-phase DCM microinverter," *IEEE Trans. Power Electron.*, vol. 33, no. 8, pp. 7229–7239, Aug. 2018.

[14] Y. Levron and R. W. Erickson, "High weighted efficiency in single-phase solar inverters by a variable-frequency peak current controller," *IEEE Trans. Power Electron.*, vol. 31, no. 1, pp. 248–257, Jan. 2016, doi: 10.1109/TPEL.2015.2399418.

[15] R. Mandrioli, A. Viatkin, M. Hammami, M. Ricco, and G. Grandi, "Variable switching frequency PWM for three-phase four-wire split-capacitor inverter performance enhancement," *IEEE Trans. Power Electron.*, vol. 36, no. 12, pp. 13674–13685, Dec. 2021, doi: 10.1109/TPEL.2021.3089610.
[16] S. Bhattacharya, S. K. Sharma, D. Mascarella, and G. Joos, "Sub-fundamental cycle switching frequency variation based on output current ripple analysis of a three-level inverter," *IEEE J. Emerg. Sel. Topics Power Electron.*, vol. 5, no. 4, pp. 1797–1806, Dec. 2017, doi: 10.1109/JESTPE.2017.2712620.
[17] D. Jiang and F. Wang, "Variable switching frequency PWM for three-phase converters based on current ripple prediction," *IEEE Trans. Power Electron.*, vol. 28, no. 11, pp. 4951–4961, Nov. 2013, doi: 10.1109/TPEL.2013.2240701.
[18] X. Mao, R. Ayyanar, and H. K. Krishnamurthy, "Optimal variable switching frequency scheme for reducing switching loss in single-phase inverters based on time-domain ripple analysis," *IEEE Trans. Power Electron.*, vol. 24, no. 4, pp. 991–1001, Apr. 2009.
[19] Y. Xia, J. Roy, and R. Ayyanar, "Optimal variable switching frequency scheme to reduce loss of single-phase grid-connected inverter with unipolar and bipolar PWM," *IEEE J. Emerg. Sel. Topics Power Electron.*, vol. 9, no. 1, pp. 1013–1026, Feb. 2021, doi: 10.1109/JESTPE.2019.2956034.
[20] H. Akagi, "Multilevel converters: Fundamental circuits and systems," *Proc. IEEE*, vol. 105, no. 11, pp. 2048–2065, Nov. 2017, doi: 10.1109/JPROC.2017.2682105.
[21] J. Rodriguez, J.-S. Lai, and F. Z. Peng, "Multilevel inverters: A survey of topologies, controls, and applications," *IEEE Trans. Ind. Electron.*, vol. 49, no. 4, pp. 724–738, Aug. 2002, doi: 10.1109/TIE.2002.801052.
[22] Z. Zhang, J. Zhang, S. Shao, and J. Zhang, "A high-efficiency single-phase T-type BCM microinverter," *IEEE Trans. Power Electron.*, vol. 34, no. 1, pp. 984–995, Jan. 2019, doi: 10.1109/TPEL.2018.2824342.
[23] G.-H. Min, K.-H. Lee, J.-I. Ha, and M. H. Kim, "Design and control of single-phase grid-connected photovoltaic microinverter with reactive power support capability," in *Proc. Int. Power Electron. Conf.*, 2018, pp. 2500–2504, doi: 10.23919/IPEC.2018.8507578.
[24] S.-J. Park, F.-S. Kang, M. H. Lee, and C.-U. Kim, "A new single-phase five-level PWM inverter employing a deadbeat control scheme," *IEEE Trans. Power Electron.*, vol. 18, no. 3, pp. 831–843, May 2003, doi: 10.1109/TPEL.ss2003.810837.
[25] Y. Xiong, S. Sun, H. Jia, P. Shea, and Z. John Shen, "New physical insights on power MOSFET switching losses," *IEEE Trans. Power Electron.*, vol. 24, no. 2, pp. 525–531, Feb. 2009, doi: 10.1109/TPEL.2008.2006567.
[26] N. Perera, A. Jafari, R. Soleimanzadeh, N. Bollier, S. G. Abeyratne, and E. Matioli, "Hard-switching losses in power FETs: The role of output capacitance," *IEEE Trans. Power Electron.*, vol. 37, no. 7, pp. 7604–7616, Jul. 2022, doi: 10.1109/TPEL.2021.3130831.
[27] M. Kasper, R. M. Burkart, G. Deboy, and J. W. Kolar, "ZVS of power MOSFETs revisited," *IEEE Trans. Power Electron.*, vol. 31, no. 12, pp. 8063–8067, Dec. 2016, doi: 10.1109/TPEL.2016.2574998.
[28] Z. Zhang, J. Zhang, and S. Shao, "A novel trapezoidal wave control method for a single-phase grid-tied T-type inverter," *IEEE Trans. Power Electron.*, vol. 36, no. 4, pp. 4711–4722, Apr. 2021, doi: 10.1109/TPEL.2020.3025965.
[29] T.-F. Wu, C.-L. Kuo, K.-H. Sun, and H.-C. Hsieh, "Combined unipolar and bipolar PWM for current distortion improvement during power compensation," *IEEE Trans. Power Electron.*, vol. 29, no. 4, pp. 1702–1709, Apr. 2014, doi: 10.1109/TPEL.2013.2265399.
[30] H. Yin, T. Lang, X. Li, S. Du, and H. Hu, "A hybrid boundary conduction modulation for a single-phase H-bridge inverter to alleviate zero-crossing distortion and enable reactive power capability," *IEEE Trans. Power Electron.*, vol. 35, no. 8, pp. 8311–8323, Aug. 2020, doi: 10.1109/TPEL.2020.2967598.
[31] H. A. Attia, T. K. S. Freddy, H. S. Che, W. P. Hew, and A. El Khateb, "Confined band variable switching frequency pulse width modulation (CB-VSF PWM) for a single-phase inverter with an LCL filter," *IEEE Trans. Power Electron.*, vol. 32, no. 11, pp. 8593–8605, Nov. 2017, doi: 10.1109/TPEL.2016.2645739.
[32] J. Zhang, T. Isobe, and H. Tadano, "Model-based control for grid-tied inverters operated in discontinuous current mode with low harmonic current distortion," *IEEE Trans. Power Electron.*, vol. 35, no. 10, pp. 11167–11180, Oct. 2020, doi: 10.1109/TPEL.2020.2978871.

Lyuyi Lin (Student Member, IEEE) received the B.S. degree in electrical engineering from Tongji University, Shanghai, China, in 2016. She is currently working toward the Ph.D. degree in electrical engineering with Zhejiang University, Hangzhou, China.

Her current research interests include control methods and optimization for high-efficiency microinverters, and differential power processing converters in photovoltaic applications.

Junming Zhang (Senior Member, IEEE) received the B.S., M.S., and Ph.D. degrees in electrical engineering from Zhejiang University, Hangzhou, China, in 1996, 2000, and 2004, respectively.

From 2010 to 2011, he was a visiting scholar with the Department of Electrical and Computer Engineering, Michigan State University, East Lansing, MI, USA. He is currently a Professor with the College of Electrical Engineering, Zhejiang University. His research interests include power electronics system integrations, power management, and high-efficiency converters.

Dr. Zhang is an Associate Editor for the IEEE TRANSACTIONS ON INDUSTRY APPLICATIONS and the *CPSS Transactions Power Electronics and Application*.

Shuai Shao (Member, IEEE) received the B.S. degree in electrical engineering from Zhejiang University, Hangzhou, China, in 2010, and the Ph.D. degree in electrical and electronic engineering from the University of Nottingham, Nottingham, U.K., in 2015.

In 2015, he was a Lecturer with the College of Electrical Engineering, Zhejiang University, where he was promoted to Associate Professor in January 2020. He authored or coauthored more than 50 peer-reviewed journal and conference papers. His research interests include solid-state transformers, bidirectional dc–dc converters, and fault detection in power converters.

Dr. Shao was a Guest Associate Editor for the IEEE JOURNAL OF EMERGING AND SELECTED TOPICS IN POWER ELECTRONICS and *CES Transactions on Electrical Machines and Systems*.